Title
Comparing Measurements of Limiting Current of Electrolytes with Theoretical Predictions up to the Solubility Limit

Journal
The Journal of Physical Chemistry C, 123(39)

ISSN
1932-7447

Authors
Shah, Deep B
Kim, Hong Keun
Nguyen, Hien Q
et al.

Publication Date
2019-10-03

DOI
10.1021/acs.jpcc.9b07121

Peer reviewed

Comparing measurements of limiting current of electrolytes with theoretical predictions up to the solubility limit

Deep B. Shah,[a,b,c] Hong Keun Kim,[d] Hien Q. Nguyen,[a] Venkat Srinivasan,[c,d] and Nitash P. Balsara[a,b,c,e,*]

[a] Department of Chemical and Biomolecular Engineering, University of California, Berkeley, California 94720, USA

[b] Materials Science Division, Lawrence Berkeley National Laboratory, Berkeley, California 94720, USA

[c] Joint Center for Energy Storage Research (JCESR), Lawrence Berkeley National Laboratory, Berkeley, California 94720, USA

[d] Argonne Collaborative Center for Energy Storage Science, Argonne National Laboratory, Lemont, Illinois 60439, USA

[e] Energy Storage and Distributed Resources Division, Lawrence Berkeley National Laboratory, Berkeley, California 94720, USA

Corresponding Author:

1* Nitash P. Balsara: E-mail: nbalsara@berkeley.edu, Address: Department of 2Chemical Engineering, 201 Gilman Hall, University of California, Berkeley, CA 394720-1462, USA, Phone: (+1) 510-642-8973.

Abstract

Imposing a steady ionic current through an electrolyte results in the formation of salt concentration gradients that compromise battery performance. The limiting current is usually defined as the current at which the salt concentration at the cathode approaches zero. Higher currents cannot be imposed on the cell as larger concentration gradients are unsustainable. We study the limiting current in electrolytes comprising a perfluorinated oligomer, C8-DMC, and lithium bis(fluorosulfonyl)imide salt in symmetric lithium cells. The time-dependence of the potential, which increases as salt concentration gradients develop, was also measured. Both steady-state and transient behaviors are modeled using Newman's concentrated solution theory; transport and thermodynamic parameters needed to perform the calculations were measured independently and reported in a previous publication [Shah et al., *Phys. Chem. Chem. Phys.,* 2019, **21**, 7857-66]. The limiting current is a non-monotonic function of salt concentration in both theory and experiment. The model shows that at low salt concentrations (below 0.88 mol/kg solvent), the concentration at the cathode approaches zero at limiting current. In contrast, at high salt concentrations (above 0.88 mol/kg solvent), the concentration at the anode approaches the solubility limit (2.03 mol/kg solvent). The experimentally determined salt concentration at which the limiting current is maximized is in excellent agreement with theoretical predictions made without resorting to any adjustable parameters.

1

Keywords

Fluorinated electrolyte, limiting current, lithium batteries, modeling, PFPE, PFE, solubility limit

1. Introduction

A barrier to the development of next-generation rechargeable lithium-based batteries is the electrolyte. Conventional electrolytes, comprising a lithium salt, $LiPF_6$, dissolved in a mixture of cyclic carbonates, exhibit limited electrochemical stability windows (< 4.5 V vs Li^+/Li), and are susceptible to thermal runaway.[1,2] One approach has been to replace conventional, carbonate electrolytes with fluorinated, electrolytes that have reduced flammability.[3–7] Fluorinated electrolytes also exhibit high oxidation potentials (> 5 V vs. Li^+/Li), and thus have the potential to enable high voltage cathodes.[8,9]

The operation of a battery results in the development of salt concentration gradients within the electrolyte. These gradients arise due to existence of two mobile charge carriers: the anion and cation, and the magnitudes of the gradients increase with increasing current density. The limiting current is defined as the largest current that can be imposed on the electrolyte. Conventional wisdom suggests that at the limiting current, the salt concentration gradient is so large that the salt concentration at the cathode approaches zero.[10] A few studies report experimentally determined liming current, but the factors that govern this parameter have not been fully elucidated.[11,12]

Complete electrochemical characterization for a binary electrolyte requires the measurement of the thermodynamic factor, T_f, and three transport properties: conductivity, κ, the salt diffusion coefficient, D, the cation transference number with respect to the solvent $t_{+¿^0¿}$.[10] All of the parameters must be measured as a function of salt concentration to obtain a complete picture.[13–17] In a recent study, Pesko et al. used measured values of T_f, κ, D, and $t_{+¿^0¿}$ in mixture of poly(ethylene oxide) (PEO) and lithium bis(trifluoromethanesulfonyl)imide salt (LiTFSI) to predict limiting current based on the conventional definition of limiting current.[18]

Recently, we reported T_f, κ, D, and $t_{+¿^0¿}$ for a perfluoropolyether, C8-DMC, mixed with lithium bis(fluorosulfonyl)imide salt (LiFSI).[19] We use Newman's concentrated solution theory to predict concentration and potential profiles as a function of salt concentration and current density in lithium symmetric cells at steady-state. We also use the theory to calculate transient concentration and potential profiles in the electrolyte. We note conditions (salt concentration and current density) under which the salt concentration at the cathode approaches zero. We also note the conditions under which salt concentration at the anode approaches the solubility limit. These predictions are compared with experimental data without the use of any adjustable parameters.

2. Experimental Details

Electrolyte Preparation

The perfluoroether, C8-DMC (CAS-No. 1976035-41-2), was synthesized from a diol terminated precursor following procedures described in previous work.[3,5,19,20] The chemical formula of C8-DMC is given in Figure 1a. All sample preparation was done within an argon filled Vac glovebox with H_2O and O_2 concentrations kept below 1 ppm. Lithium bis(fluorosulfonyl)imide (LiFSI) (cat. no. 097602) was purchased from Oakwood Products, Inc. Figure 1b contains the chemical formula of the FSI anion. The salt was ≥ 99% pure, as confirmed by a Certificate of Analysis form. The salt was dried at 100 °C under dynamic vacuum for three days inside a glovebox antechamber. Prior to transfer into the glovebox, C8-DMC was dried under active vacuum inside the glovebox antechamber at 50 °C for 72 hours. In order to form electrolytes, a predetermined amount of Li salt was added to a known mass of C8-DMC. Once the salt was added, the electrolytes were placed on a magnetic stirrer and were allowed to mix for 12 hours or more using a magnetic stir bar. The salt concentration of prepared electrolytes is described as m_{av}, the molality of the electrolyte in units of mol LiFSI/kg C8-DMC. Electrolytes were prepared within a concentration window of $0.28 \leq m_{av} \leq 1.78$ mol/kg.

(a) (b)

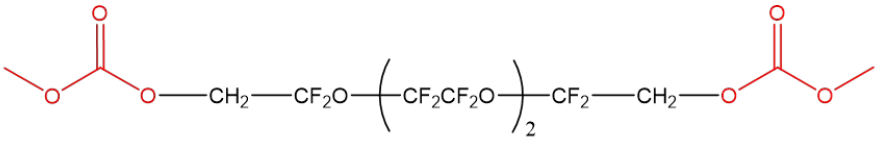

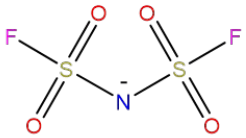

Figure 1: (a) C8-DMC and (b) FSI anion.

Lithium symmetric cells and limiting current measurements

Lithium symmetric cells were assembled by sandwiching an electrolyte-soaked separator, Celgard 2500 (Celgard Company), with lithium discs, cut from lithium chips (MTI Corp.). Celgard 2500 was cut to 19 mm in diameter and had an average thickness, L, of 25.4 ± 0.6 μm. The diameter of the 150 µm thick Li disc was 12.7 mm. Three replicate cells were produced for each electrolyte and the reported data is the average of those three cells, with error bars representing the standard deviation between the replicate cells. Data were collected on a Bio-Logic VMP3 potentiostat. Each sample cell was subjected to a conditioning treatment, which consisted of charge and discharge cycles at 0.02 mA/cm^2 in order to help stabilize the interfacial layer. The sequence performed was a 4 hour charge, 30 minutes rest, a 4 hour discharge, 30 minutes rest, and repeated for a total of 6 times. To track the cell impedance with time, ac impedance spectroscopy was performed before the beginning of conditioning, after each rest step, and at the end of conditioning. Complex impedance plots were obtained within a frequency range of 1 MHz to 100 mHz. Each sample was then polarized at all of the following current densities for 30 minutes: i_{ss} = 0.20, 0.40, 0.50, 0.60, 0.70,

10.75, 0.80, and 1.00 mA/cm^2 with potential and current data recorded every 2five seconds. Ac impedance spectroscopy followed each polarization and the 3data were analyzed in the form of a Nyquist plot. The data were fit to an 4equivalent electrical circuit and the interfacial impedance, R_i, was extracted, 5as described in a previous publication.[5] The interfacial impedance was used 6to correct for the potential drop, Φ, across an electrolyte, as described in Eq. 71 below

$$\Phi(t)=\Phi_{measured}(t)-R_i i_{ss} A \quad (1)$$

8

9where $\Phi_{measured}$ is the potential across the lithium symmetric cell as measured 10by the potentiostat under a given steady-state current density, i_{ss}, and A is 11the active area of the electrode. All electrochemical characterization was 12done at 30 C.

13

14**3. Theory**

15*Steady-state model*

16The relationship between i_{ss} and the electrochemical properties of an 17electrolyte, based on Newman's concentrated solution theory,[10] was derived 18in ref. 18. This relationship changes slightly when the electrolyte is contained 19in a porous separator (we call this the electrolyte/separator composite), and 20is given by Eq. 2

$$\int_{m(x=0)}^{m(x)} \frac{c(m)D_s(m)}{mt_{-¿^0(m)}}dm=\frac{i_{ss}L}{Fz_{-¿}v_{-¿}\left(\frac{x}{L}\right)¿}¿ \quad (2)$$

where c is the concentration of the salt in the electrolytic phase in mol/cm^3, D_s is the salt diffusion coefficient measured by restricted diffusion on the electrolyte/separator composite, m is the molality, $t_{-,0}$ is the anion transference number relative to the velocity of the solvent ($t_{-,0}=1-t_{+,0}$), z_- is the charge number on the anion, v_- is the number of anions the salt disassociates into, L is the thickness of the electrolyte/separator composite, x/L is the normalized thickness, and F is Faraday's constant (the transference number is unaffected by the presence of the separator). All of the ion transport properties depend on salt concentration, as indicated in Eq. 2. During an experiment, the average salt concentration of the electrolyte, m_{av}, is controlled. The molality profile predicted by Eq. 2 must be averaged from $x = 0$ to $x = L$ to ensure that the model predicted average concentration is equal to m_{av}.

The relationship between the electric potential within an electrolyte/separator composite to the measurable transport properties is given by

$$\Phi_{ss}(x)=-F z_- v_- \int_{m(x=L)}^{m(x=0)} \frac{c(m)D_s(m)}{m t_{+,id}(m)\kappa_s(m)\left(1-t_{+,0}(m)\right)}dm \qquad (3)$$

where $t_{+,id}$ is the ideal transference number (unaffected by the presence of the separator) and κ_s is the conductivity of the electrolyte/separator

composite. The ideal transference number, $t_{+,id}$, is determined by the steady-state current method.[21,22] The relationship between the ideal transference number and κ, $t_{-,0}$, $1+\frac{d\ln\gamma_{\pm}}{d\ln m}$ (the thermodynamic factor), and D is given in ref. 23 and a relationship was first noted in ref. 24. In this paper, Eqs 2 and 3 were solved numerically using MATLAB and published data[19] for the relevant parameters.

Transient model

As is the case for the steady-state model, the transient model is also based on Newman's concentrated solution theory.[10] We solve the governing differential equation along the thickness direction (denoted as the x-direction in the present analysis) of the polymer electrolyte. Since lithium metal exists on both ends of the electrolyte domain, these lithium/polymer interfaces have been considered as the two boundaries of the one-dimensional computational domain. Table 1 summarizes the governing equations and boundary conditions used in this study. The mass balance relation for electrolyte salt is expressed in Eq. 4, which was derived based on concentrated solution theory, is used to obtain transient concentration profiles $\left(c\left(x,t\right)\right)$ across the polymer electrolyte. Note that the effect of transference number gradient is also taken into account, as shown in the second term on the right of Eq. 4. The modified Ohm's law expressed in Eq. 7, which includes the polarization in the electrolyte due to concentration

gradients, is used to obtain transient ionic potential profiles, $\Phi_1(x,t)$, across the polymer. The potential drop across the polymer electrolyte is denoted as $\Phi_{1,(x=0)}-\Phi_{1,(x=L)}$. The model parameters used in this study are listed in Table 2.

Table 1: Summary of governing equations for C8-DMC/LiFSI with a Celgard 2500 separator in a Li symmetric cell

	Governing equation	Boundary conditions
Mass balance (polymer electrolyte)	$\frac{\partial c}{\partial t}=\nabla\bullet\left[D_S\left(1-\frac{d\ln c}{d\ln c_0}\right)\nabla c\right]-i_{ss}\bullet\nabla$ (4)	$-D_s\frac{\partial c}{\partial x}\Big\|_{x=0}=1-\frac{t_{+¿^0}}{F}i_{ss}¿$ (5) $-D_s\frac{\partial c}{\partial x}\Big\|_{x=L}=-1-\frac{t_{+¿^0}}{F}i_{ss}¿$ (6)
Modified Ohm's law (Ionic phase)	$i_{ss}=-\kappa_S\nabla\Phi_2+\frac{2\kappa_s RT}{F}\left(1+\frac{\partial\ln f_{\pm}}{\partial\ln c}\right)¿$ (7)	$\Phi_{2,L}=0$ (8)

Table 2: Parameters used for Li symmetric transient modeling of C8-DMC/LiFSI with a Celgard 2500 separator

Symbol	Parameter	Initial Value	Reference
L	Thickness of separator	2.54e-3 [cm]	Measured
κ	Ionic conductivity of C8-DMC	Function of concentration	Measured
D	Diffusion coefficient of LiFSI in C8-DMC	Function of concentration	Measured
$t_{+¿^0¿}$	Cation transference number	Function of concentration	Measured
F	Faraday constant	96450 [C/mol]	-
R	Universal gas constant	8.314 [J/mol/K]	-
T	Temperature	30 [°C]	-

4. Results and Discussion

Our objective is to compare potential versus time curves determined experimentally in Li symmetric cells as a function of average salt concentration and current density up to the salt solubility limit and the limiting current with theoretical predictions. Table 3 shows the aforementioned transport and thermodynamic properties of

electrolyte/separator composites for a range of salt concentrations taken from ref. 19. It is convenient to work with units of molality for steady-state calculations while transient calculations are best done using molar concentrations. In Table 3, we list both *m* and *c*, based on measurements reported in ref. 19. Note that $t_{+,0}$ is negative over the entire concentration range, indicating the formation of charged clusters. The interactions that lead to the formation of these clusters has not yet been elucidated.

Table 3: Transport properties of C8-DMC/LiFSI with a Celgard 2500 separator at 30 °C[19]

m (mol/kg)	*c* (mol/cm^3)	κ_s (S/cm)	D_s (cm^2/s)	$t_{+,id}$	$t_{+,0}$	$1+\frac{d\ln\gamma_{\pm}}{d\ln m}$
0.28	3.87×10^{-4}	$[2.91 \pm 0.19] \times 10^{-6}$	$[3.66 \pm 0.39] \times 10^{-8}$	0.89 ± 0.01	-1.002 ± 0.06	0.15 ± 0.02
0.60	8.89×10^{-4}	$[9.82 \pm 0.90] \times 10^{-6}$	$[2.24 \pm 0.12] \times 10^{-8}$	0.77 ± 0.01	-0.751 ± 0.04	0.19 ± 0.02
0.94	1.36×10^{-3}	$[1.17 \pm 0.07] \times 10^{-5}$	$[1.72 \pm 0.13] \times 10^{-8}$	0.71 ± 0.07	-0.378 ± 0.04	0.42 ± 0.06
1.30	1.70×10^{-3}	$[1.14 \pm 0.09] \times 10^{-5}$	$[1.34 \pm 0.11] \times 10^{-8}$	0.67 ± 0.02	-0.070 ± 0.00	0.85 ± 0.11
1.78	2.36×10^{-3}	$[7.92 \pm 0.75] \times 10^{-6}$	$[1.20 \pm 0.21] \times 10^{-8}$	0.67 ± 0.02	-0.232 ± 0.01	1.12 ± 0.23

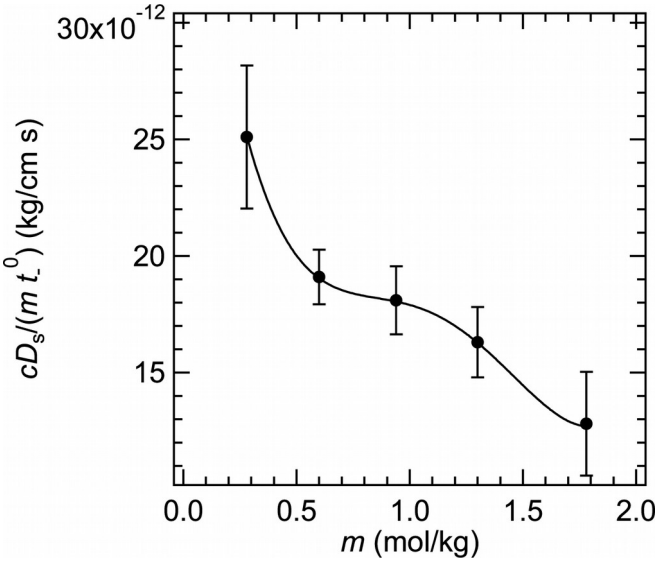

Figure 2: Fit of the integrand term of Eq. 2, $\frac{cD_s}{mt_{-}^0}$, with LiFSI salt molality. The solid curve shows the least-squares polynomial fit given by Eq. 9.

To calculate the concentration profile within an electrolyte given a steady-state current density, i_{ss}, and thickness, L, the transport parameters given in Table 3 were fit as a continuous function to salt concentration. In Figure 2, we show the 4th order polynomial fit to the product appearing on the right side of Eq. 2,

$$\frac{c(m)D_s(m)}{mt_{-}^0(m)=k_0+k_1m+k_2m^2+k_3m^3+k_4m^4} \quad (9)$$

with fitting parameters

$$k_0=2.03\,x\,10^{-10} \quad k_1=-4.52\,x\,10^{-10} \quad k_2=6.46\,x\,10^{-10}$$
$$k_3=-3.99\,x\,10^{-9} \quad k_4=8.861\,x\,10^{-11}$$

where t_{-}^0 is equal to $1-t_{+}^0$, D_s is in cm^2/s, c is in mol/cm^3, and m is in mol/kg. The parameters apply to the range $0.28 \le m \le 1.78$ mol/kg and for T = 30 °C.

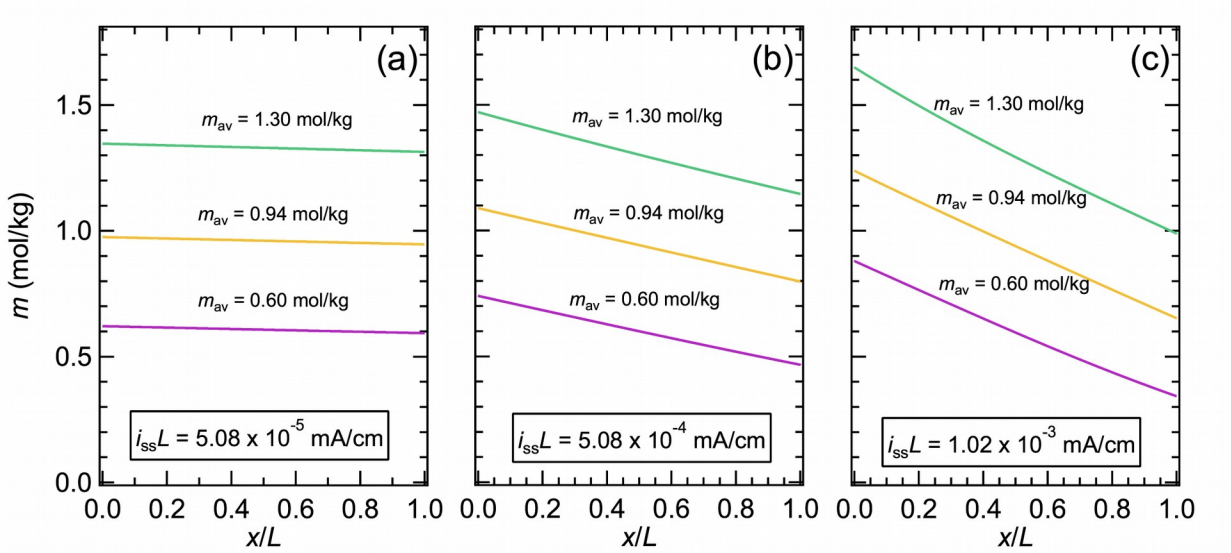

Figure 3: Concentration profiles of LiFSI in C8-DMC predicted by Eq. 2 at steady-state for three different normalized current densities: (a) $i_{ss}L$ = 5.08 x 910^{-5}, (b) $i_{ss}L$ = 5.08 x 10^{-4}, and (c) $i_{ss}L$ = 1.02 x 10^{-3} mA/cm.

Fig. 3 shows the concentration profiles across a mixture of C8-DMC/LiFSI for three initial concentrations of m_{av} = 0.60, 0.94, and 1.30 mol/kg and for three values of normalized current density, $i_{ss}L$. We have chosen the product $i_{ss}L$ for this plot because i_{ss} is inversely proportional to L; Fig. 3 may thus be used to determine i_{ss} values for L values different from that used in this particular study. The concentration profiles were obtained by numerically solving Eq. 2 using the fitted Eq. 4. The figures correspond to $i_{ss}L$ = 5.08 x 10^{-5}, 5.08 x 10^{-4}, and 1.02 x 10^{-3} mA/cm (relating to i_{ss} = 0.02, 0.20, and 0.40

1mA/cm^2 for L = 0.00254 cm). It is evident from Fig. 3a that under small
2applied normalized current densities ($i_{ss}L$ = 5.08 x 10^{-5} mA/cm), the
3concentration profiles are approximately linear and the gradients are small.
4However, with increasing normalized current densities, the concentration
5gradients become steeper, as shown in Figs. 3b and c. Note that the overall
6flux of lithium cations, at steady-state, is toward the negative electrode in
7spite of the fact that the transference number is negative at all salt
8concentrations. The sign of the transference number only gives the direction
9of the flux of lithium cations in a solution of uniform composition in response
10to an applied electrochemical potential. Thus, at the instant that a dc
11potential is applied to the cell, the net lithium cation flux is toward the
12positive electrode. At steady-state after the salt concentration gradients are
13fully developed, the net lithium cation flux is toward the negative electrode.[25]
14
15One can estimate the normalized limiting current, $i_{limit}L$, within an electrolyte
16using model predicted concentration profiles. In order to do so, an electrolyte
17of known m_{av} must be modeled under a number of $i_{ss}L$ values and the salt
18concentration at the cathode (x/L = 1) is extracted at each normalized
19current density. An example of such an analysis is shown in Fig. 4a. In Fig.
204a, $i_{ss}L$ is plotted against the model predicted salt concentration, m, at x/L =
211 in blue circles for an electrolyte with an average salt concentration of m_{av}
22= 0.94 mol/kg. As the model is limited between 0.28 $\leq m \leq$ 1.78 mol/kg, the
23conventional limiting current must be predicted by extrapolating m(at x/L =

11) to zero. The dashed, black curve is a 2nd order polynomial fit to the model 2predicted values in Fig. 4a, and predicts $i_{limit}L$ = 3.7 x 10^{-3} mA/cm. It should 3be noted that the solubility limit of LiFSI in C8-DMC is 2.03 mol/kg.[5] It is 4obvious that the concentration at any x/L in the cell must not exceed this 5value for stable operation. The highest salt concentration occurs at the 6anode (x/L = 0). In Fig. 4b, we thus plot $i_{ss}L$ versus $m(x/L = 0)$ for the same 7average salt concentration used in Fig. 4a (m_{av} = 0.94 mol/kg). A 2nd order 8polynomial is fit through the data and extrapolated to m = 2.03 mol/kg is 9shown as a dashed curve. We define the normalized limiting current at which 10this occurs as $i_{limit,sat}L$ which is 3.2 x 10^{-3} mA/cm for m_{av} = 0.94 mol/kg.

11

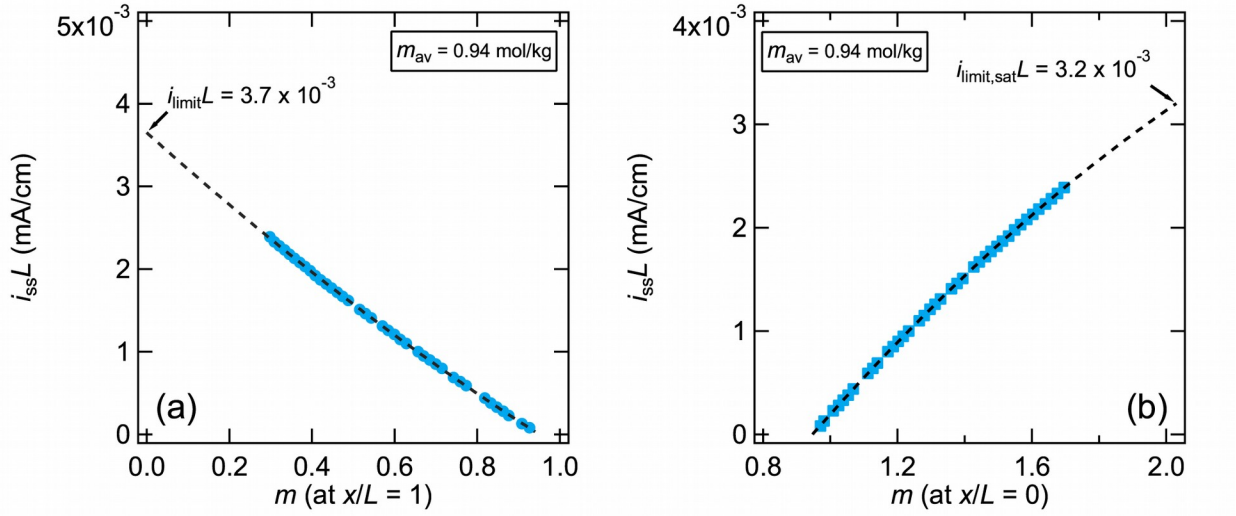

12

13**Figure 4:** Concentration predictions at the anode (x/L = 1) and cathode (x/L 14= 0) for varying $i_{ss}L$ values for an electrolyte with an average concentration 15of m_{av} = 0.94 mol/kg. (a) Model predictions of the concentration at the 16anode, x/L = 1. The black dashed curve shows the least-squares polynomial 17fit, which was extrapolated to m = 0 mol/kg to determine the normalized 18limiting current density (marked as $i_{limit}L$). (b) Model predictions of the 19concentration at the cathode, x/L = 0. The black dashed curve is a least-20squares polynomial fit, which was extrapolated to the salt solubility limit of

m = 2.03 mol/kg. This determined the normalized limiting current density caused by salt saturation at the cathode (marked as $i_{limit,sat}L$).

There is an important question: for a given m_{av}, which mode of the limiting current will be observed? We posit that the mode will correspond to the one that is obtained at the lower normalized limiting current. For m_{av} = 0.94 mol/kg, we conclude that the normalized limiting current will occur due to salt precipitation. Similar analysis was repeated at all values of m_{av}.

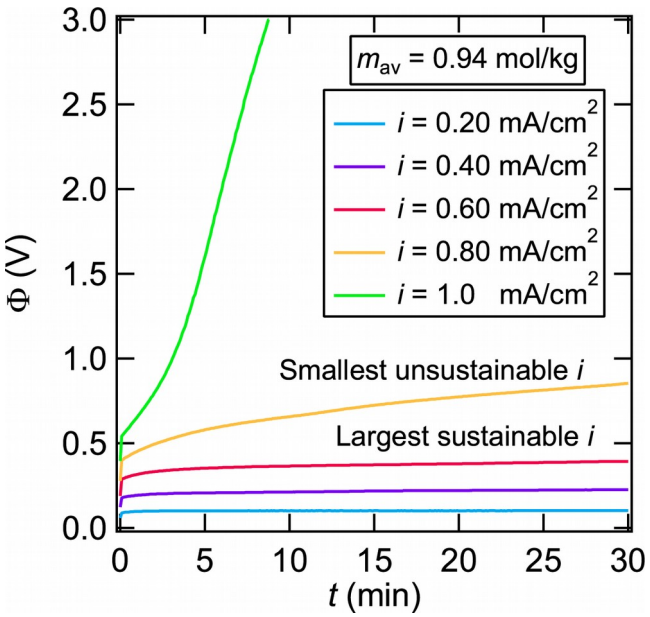

Figure 5: Time dependent potential behavior of C8-DMC/LiFSI with an average salt concentration of m_{av} = 0.94 mol/kg in response to applied current densities from i = 0.20 to 1.0 mA/cm^2 (no interfacial impedance correction). The largest sustainable current density, i, as determined by plateau in measured potential, was 0.60 mA/cm^2, shown as a solid red curve. The smallest unsustainable i, as determined by the lack of a plateau in the potential within the measurement window, was 0.80 mA/cm^2 and is shown as a solid yellow curve.

Turning to experiments, we now discuss potential versus time curves for an electrolyte/separator composite in a lithium symmetric cell (L = 0.00254 cm)

at a fixed applied current. In Fig. 5, we show the potential profile versus time for current densities ranging from i_{ss} = 0.20 mA/cm^2 to 1.00 mA/cm^2 in 0.2 mA/cm^2 increments for an initial concentration of m_{av} = 0.94 mol/kg. At low current densities (below 0.60 mA/cm^2), the potential increases instantaneously at $t = 0^+$ due to the resistance of the cell when concentration is uniform, increases with time as concentration gradients develop, and reaches a plateau when the concentration profile in the cell approaches steady-state. At a slightly higher current density of 0.80 mA/cm^2, the potential increases monotonically with time and does not reach a plateau. We refer to 0.60 mA/cm^2 as the largest sustainable current density and 0.80 mA/cm^2 as the smallest unsustainable current density. Increasing the current density beyond 0.80 mA/cm^2 leads to potential increases exponentially with time with no hint of a plateau. Data similar to that shown in Fig. 5 was obtained for all of the electrolytes. The normalized limiting current density, $i_{limit}L$, was determined for each electrolyte by averaging the largest sustainable current and smallest unsustainable current. In Fig. 6, we plot the experimental limiting current, $i_{limit}L$, as a function of m_{av}. The normalized limiting current for m_{av} = 0.28 mol/kg is 1 x 10^{-3} mA/cm. It increases with increasing salt concentration, reaching a broad maximum of $i_{limit}L$ = 1.8 x 10^{-3} mA/cm between m_{av} = 0.60 and 0.94 mol/kg. Further increase in m_{av} results in a decrease in $i_{limit}L$ until m_{av} = 1.78 mol/kg, a value that is close to the salt solubility limit.

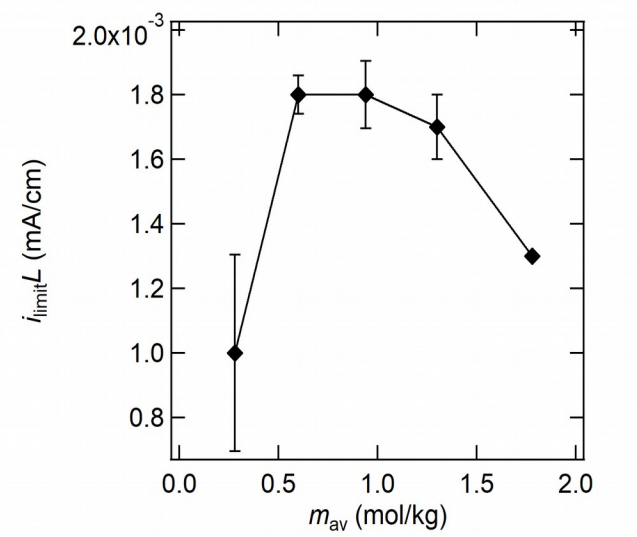

Figure 6: Experimental limiting current as a function of salt concentration. The limiting current was taken as the average between the largest sustainable current and smallest unsustainable current. The solid line is drawn to guide the eye.

In Fig. 7a, $i_{limit}L$ is plotted against m_{av}; the black diamonds show experimental measurements that were shown in Fig. 6, red squares represent the predicted $i_{limit}L$ when concentration reaches zero at the cathode ($x/L = 1$), and blue circles are the predicted $i_{limit}L$ values when the solubility limit of m = 2.03 is reached at the anode ($x/L = 0$). The cathode-dominated $i_{limit}L$ (the traditional limiting current) increases with increasing concentration. In contrast, the anode-dominated $i_{limit,sat}L$ decreases with increasing concentration. The two normalized limiting currents are equal to each other at m_{av} = 0.88 mol/kg. Following our assumption that the failure mode obtained experimentally corresponds to the one that requires the lower current density, we conclude that salt depletion at the cathode causes the limiting current at $m_{av} < 0.88$ mol/kg, while salt precipitation at the anode causes the limiting current at $m_{av} > 0.88$ mol/kg. The two solid curves

through the theoretical predictions in Fig. 7a show these two branches. The theoretical predictions provide a qualitative explanation for the observed non-monotonic dependence of the measured limiting current on salt concentration. There are two important quantitative differences between theory and experiment in Fig. 7a: (1) The theoretical limiting currents are about a factor of 2 higher than those measured experimentally and (2) The peak in the limiting current versus salt concentration predicted by theory is sharper than that observed experimentally. We do not have definitive explanations for these deviations, except to note that the interface between the electrode and electrolyte is complex, and that failure in the experimental cells may begin before the salt concentration at the cathode reaches zero or the salt concentration at the anode reaches the solubility limit.

Approximate expressions are often used to determine the normalized limiting current due to salt depletion at the cathode. [26–28] One such expression can be derived by combining equations 11.22, 11.41, 11.43, and 11.57 in ref. 10:

$$i_{limit} L = \frac{2 c_{av} D_S F}{1 - t_{+,id}} \qquad (10)$$

where c_{av} is the average electrolyte concentration in mol/cm^3, D_s is the restricted diffusion coefficient in the electrolyte/separator composite, and we have taken the liberty of using the $t_{+,id}$. Similarly, the normalized limiting

current that causes the concentration at the anode to approach the solubility limit is:

$$i_{limit,sat}L = 2\frac{(c_{sat} - c¿¿av)D_s F}{1 - t_{+,id}}¿ \quad (11)$$

where c_{sat} is salt solubility limit. For mixtures of C8-DMC and LiFSI, c_{sat} = 2.61 x 10^{-3} mol/cm^3. Equations 10 and 11 were derived using dilute solution theory, thus the ideal transference number, $t_{+,id}$, is used in both equations. In Fig. 7b, we plot $i_{\text{limit}}L$ vs. m_{av}; red squares denote the predicted $i_{\text{limit}}L$ using Eq. 10, and blue circles represent the predicted $i_{\text{limit,sat}}L$ using Eq. 11. Both predictions for the normalized limiting current decrease with increasing salt concentration. The cross-over from the salt-depletion limit to the salt precipitation limit occurs at a reasonable value of m_{av}, but the predicted trend is monotonic with salt concentration and inconsistent with the experimental data. In addition, the theoretical predictions for normalized limiting current based on dilute solution theory are an order of magnitude higher than those measured experimentally (black squares in Fig. 7b). It is obvious from Fig. 7 that concentrated solution theory is essential for establishing the underpinnings of the normalized limiting current in our system.

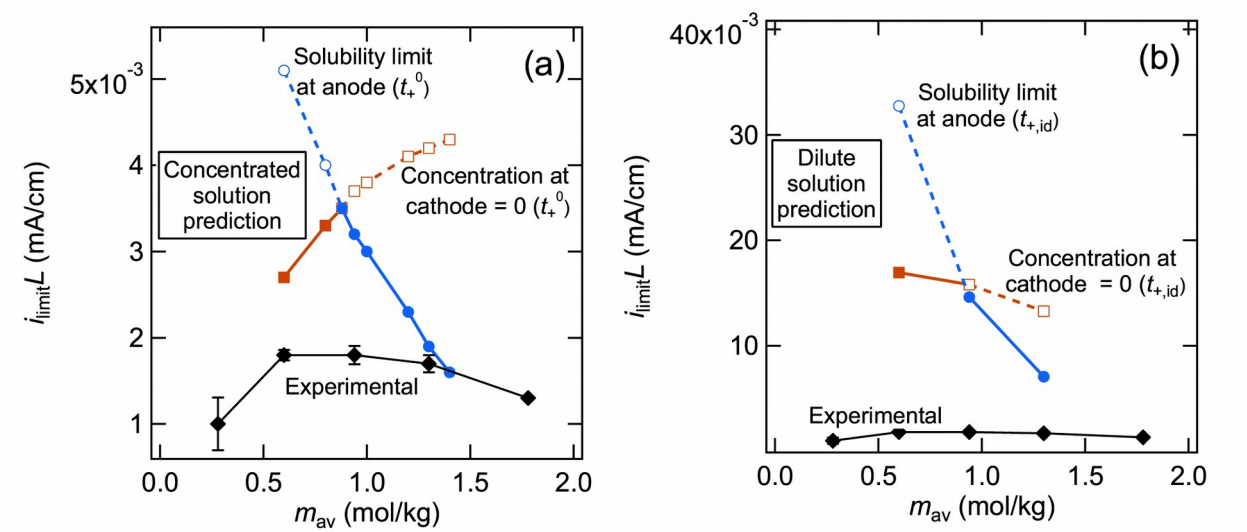

Figure 7: Normalized limiting current predictions as a function of m_{av} and compared to experimental values (shown in black). (a) Concentrated solution theory predictions of the normalized limiting current. The red dashed and solid curves are the $i_{limit}L$ predicted when extrapolating m_{av} to 0 mol/kg at the cathode (x/L = 1). The blue dashed and solid curves are the $i_{limit,sat}L$ predicted by extrapolating m_{av} to 2.03 mol/kg at the anode (x/L = 0). (b) Normalized limiting current predictions using dilute solution theory. The red dashed and solid curves are the $i_{limit}L$ predicted by Eq. 10 (concentration equal to 0 mol/cm^3 at the cathode). The blue dashed and solid curves are the $i_{limit,sat}L$ predicted by Eq. 11 (salt saturation at the anode, c_{sat} = 2.61 x 10^{-3} mol/cm^3). Normalized limiting current predictions using dilute solution theory are an order of magnitude higher than the experimental values.

We now return to the potential that can be predicted using Eq. 3. In Fig. 8, we plot the integrand in Eq. 3 along with a fit to the following empirically determined function:

$$\frac{c(m)D_s(m)}{mt_{+,id}(m)\kappa_s(m)t_{-,0}(m)} = b_0\exp(-\tau_3 m) + b_1\exp(-\tau_4 m) \quad (12)$$

with fitting parameters

$$b_0 = 1.802\,x\,10^{-6} \quad b_1 = 8.566\,x\,10^{-5}$$
$$\tau_3 = 0.1541 \quad \tau_4 = 8.525$$

where κ_s is the conductivity of the separator/electrolyte composite in S/cm.

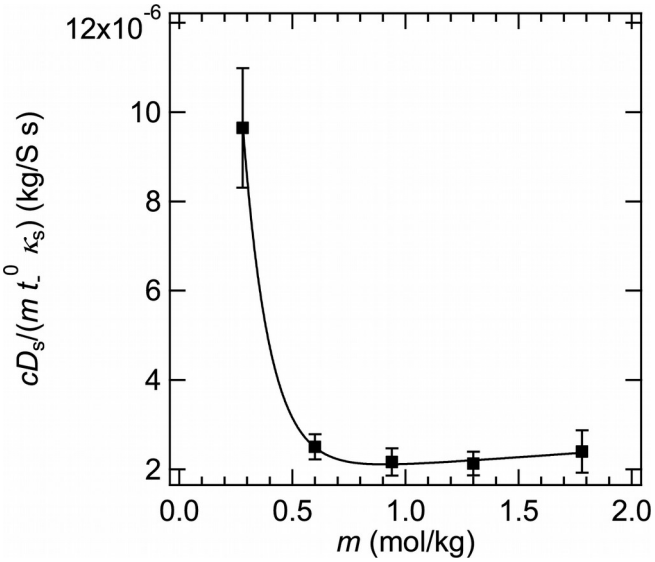

Figure 8: Fit of the integrand term of Eq. 3, $\frac{cD_s}{mt_{+,id}\kappa_s t_{-}^{0}}$, with LiFSI salt molality. The solid curve shows the least-squares fit to the double exponential given by Eq. 7.

The fit from Fig. 8 allows for potential predictions across the C8-DMC/LiFSI electrolyte. In Fig. 9, we show the predicted potential profile, $\Phi(x/L)$, across the electrolyte from x/L = 0 to 1 for selected values of m_{av} and $i_{ss}L$. We define Φ = 0 at x/L = 1. The purple, yellow, and green solid curves are potential profiles for m_{av} = 0.60, 0.94, and 1.30 mol/kg, respectively. From left to right, each figure provides profiles for $i_{ss}L$ = 5.08 x 10^{-5}, 5.08 x 10^{-4}, and 1.02 x 10^{-3} mA/cm, respectively. Note that these values of $i_{ss}L$ correspond to the applied i_{ss} in our cell equal to 0.02, 0.20, and 0.40 mA/cm^2 (L = 0.00254 cm). At $i_{ss}L$ = 5.08 x 10^{-5} mA/cm, the potential profile across the electrolyte is linear and the gradient is small, as shown in Fig. 9a, but the potential behavior

becomes less linear with increasing $i_{ss}L$. Interestingly, the intermediate concentration of m_{av} = 0.94 mol/kg shows a lower $\Phi(x)$ across the electrolyte at all values of $i_{ss}L$, compared to m_{av} = 0.60 or 1.30 mol/kg. The potential drop for m_{av} = 0.60 shows more complex behavior: it has a lower potential drop across the electrolyte when compared to m_{av} = 1.30 at both $i_{ss}L$ = 5.08 x 10^{-5} and 5.08 x 10^{-4} mA/cm, but has the largest potential drop across the electrolyte at $i_{ss}L$ = 1.02 x 10^{-3} mA/cm. Next, we compare the model predicted potential drop across the electrolyte to experimental measurements of potential, Φ_{exp}, for a range of m_{av}. The experimentally accessible potential is at x/L = 0. We thus define Φ_0 as to be the theoretically predicted potential at x/L = 0 for a given m_{av} and i_{ss}.

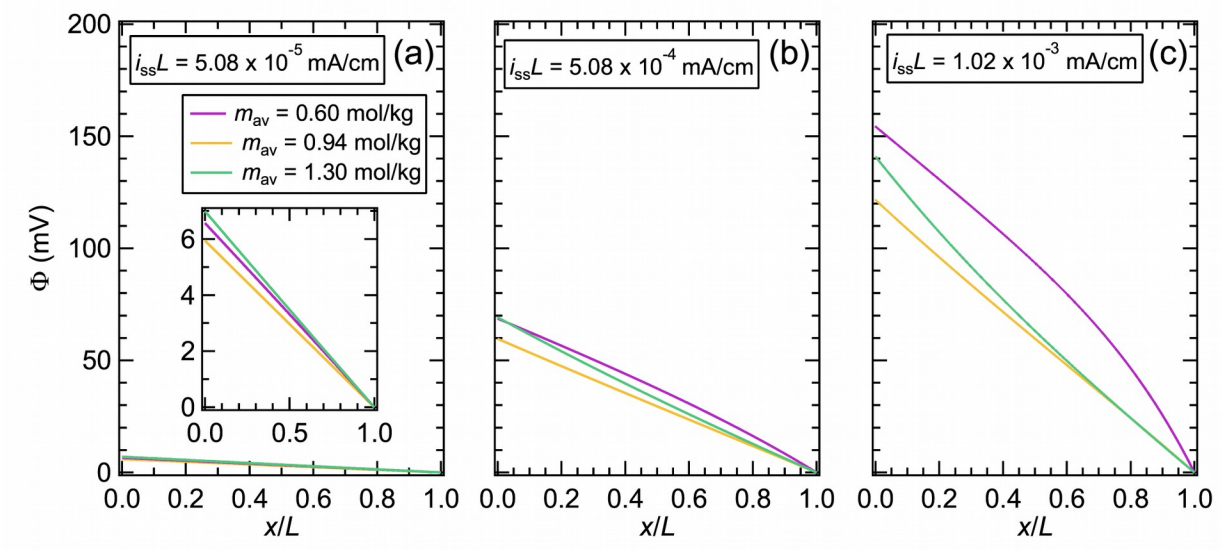

Figure 9: Potential profiles in C8-DMC/LiFSI electrolytes predicted by concentrated solution theory at steady-state. These are calculated using Eq. 3 based on the fit shown in Fig. 8. Potential profile for (a) $i_{ss}L$ = 5.08 x 10^{-5} mA/cm, (b) $i_{ss}L$ = 5.08 x 10^{-4} mA/cm, and (c) $i_{ss}L$ = 1.02 x 10^{-3} mA/cm. Interestingly, the potential drop across C8-DMC/LiFSI with m_{av} = 0.60 at $i_{ss}L$

1= 5.08 x 10^{-5} mA/cm is less than that of m_{av} = 1.30, but has a higher
2potential drop at $i_{ss}L$ = 1.02 x 10^{-3} mA/cm.
3
4The experimentally applied potential drop, Φ_{exp}/L, for the electrolyte with m_{av}
5= 0.94 mol/kg is plotted as a function of i_{ss} in Fig. 10a. The experimental
6potential drop is corrected for the lithium/electrolyte interfacial impedance
7using Eq. 1. Also shown in Fig. 10a is the predicted potential drop, Φ_0/L,
8calculated from Fig. 9 for m_{av} = 0.94 mol/kg. Both theory and experiment
9indicate that Φ/L increases with increasing i_{ss}. At i_{ss} = 0.20 mA/cm^2, the
10theoretically predicted potential drop, Φ_0/L, is within experimental error. The
11deviation between experiments and theory increases with increasing current
12density. Further work is needed to resolve this discrepancy. In Fig. 10b, we
13plot Φ_{exp}/L versus m_{av} for i_{ss} = 0.4 mA/cm^2. Φ_{exp}/L is a weak function of m_{av}.
14Theoretical predictions, also shown in Fig, 10b, support this observation.
15While the theoretical predictions generally lie below the experimental data,
16they are within experimental error at m_{av} = 0.60 and 1.30 mol/kg.
17

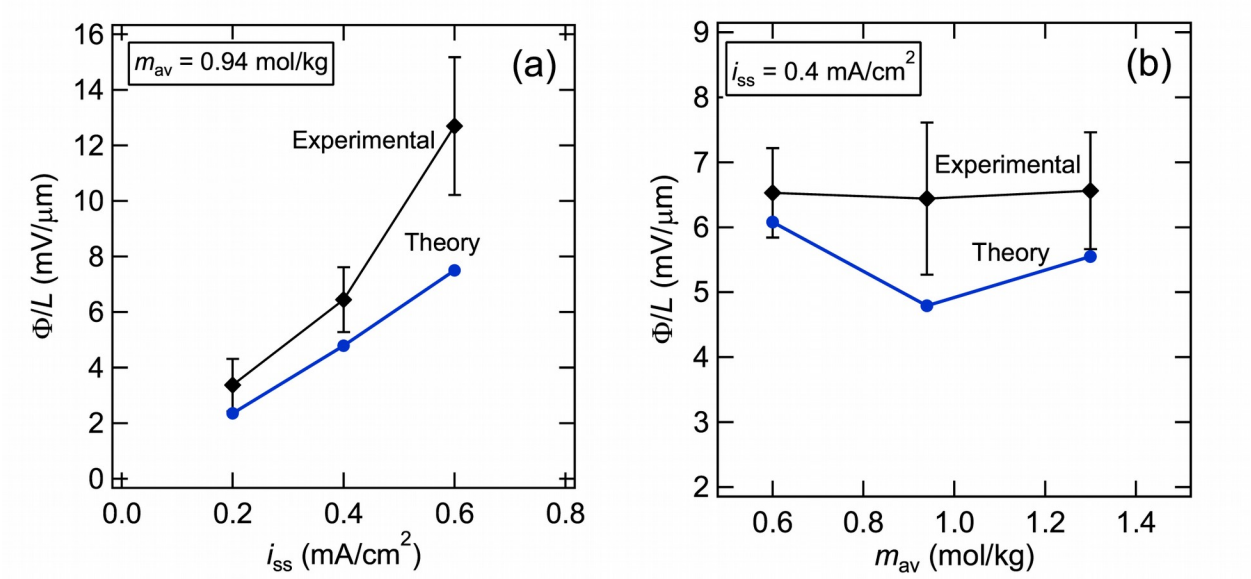

Figure 10: Experimental (black) and model predicted (blue) potential as a funtion of (a) i_{ss} for a concentration of m_{av} = 0.94 mol/kg and (b) m_{av} for i_{ss} = 40.40 mA/cm^2.

Figure 11 shows the comparison between the experimentally measured and predicted time evolution of cell potential based on the transient model (Table 1) using the same thermodynamic and transport parameters used in the analysis of steady-state data presented in Figs. 2-10. The transient model, as described in Table 1, is used for the numerical predictions of cell potential for different average salt concentrations of m_{av} = 0.60 mol/kg (c_{av} = 8.89 x 10^{-4} mol/cm^3), m_{av} = 0.94 mol/kg (c_{av} = 1.36 x 10^{-3} mol/cm^3), and m_{av} = 1.30 mol/kg (c_{av} = 1.70 x 10^{-3} mol/m^3). The experimental results, denoted by the solid curves, are obtained from averaged potentials measured from three separate cells; whereas, the highlighted regions show the range of measured potentials across the cells. The dashed curves indicate the transient model results. As shown in Figure 11a and b, the transient model predictions are in quantitative agreement with experiments at all applied current densities for

m_{av} = 0.60 and 0.94 mol/kg. The theoretical and experimental potential jumps at $t = 0^+$ are in agreement, as is the approach to steady-state wherein the cell potential increases with time as concentration gradients develop. The agreement between theory and experiment is only qualitative at m_{av} = 1.30 mol/kg (Figure 11c). While the time-scale over which concentration gradients develop are similar in both theory and experiment, both the instantaneous potential at $t = 0^+$ and the steady-state potential measured experimentally are higher than theoretical predictions. While it is not clear why this discrepancy is seen at m_{av} = 1.30, the agreement between the model and the data seen in Figure 11 is noteworthy, as there are no adjustable parameters in the model.

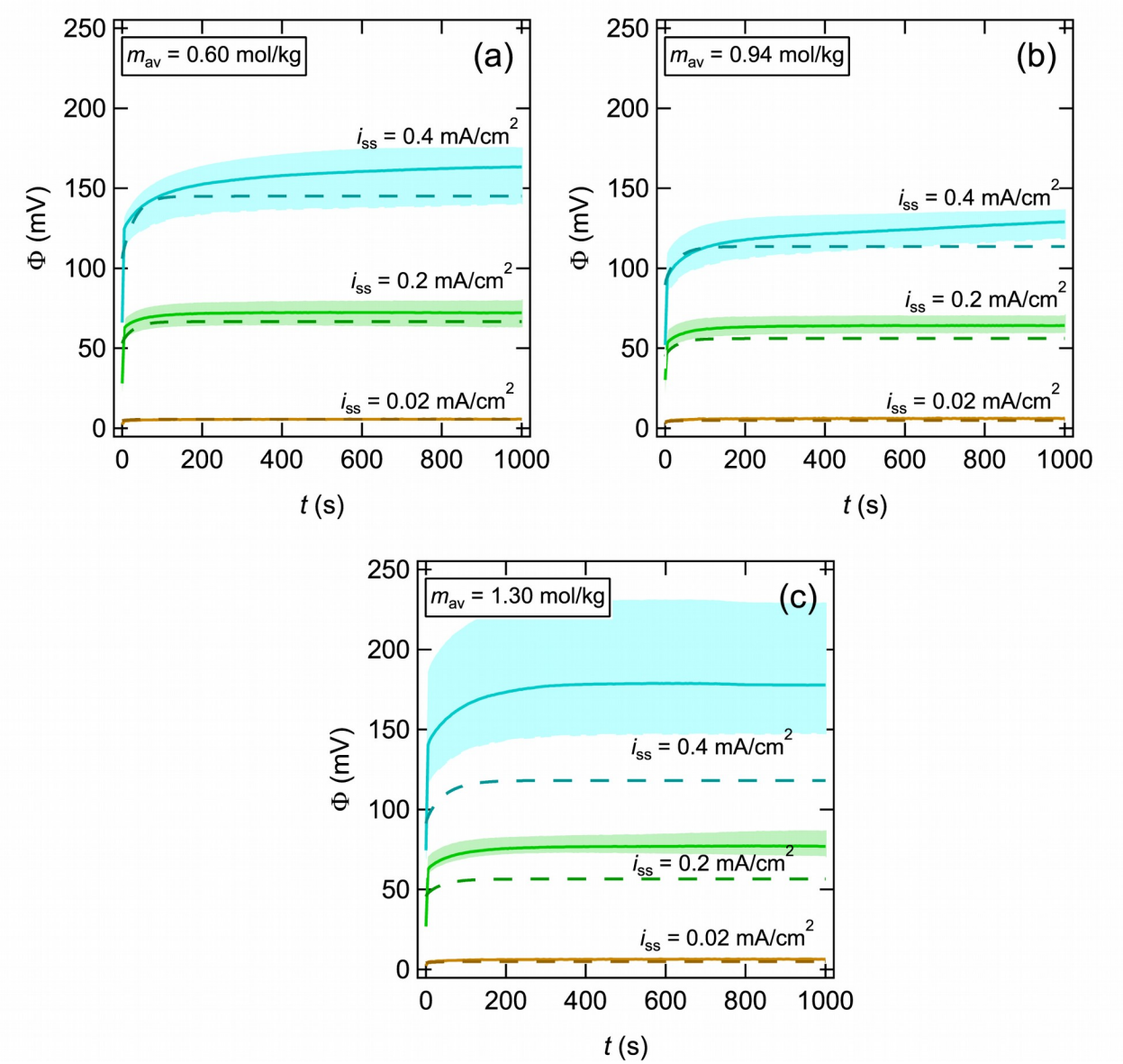

Figure 11: Time dependent experimental potentials (solid curves) are compared to our transient model (dashed curves) for litihium symmetric cells. The experimental data was averaged from three replicate cells (solid curves) and the error is given by the standard deviation (light shaded areas). Transient potential behavior for i_{ss} = 0.02, 0.20, and 0.40 mA/cm^2 for (a) m_{av} = 0.60 mol/kg, (b) m_{av} = 0.94 mol/kg, and (c) m_{av} = 1.30 mol/kg.

5. Conclusion

The performance of an electrolyte in a battery is limited, in part, by the maximum current that can be drawn through it. Traditionally, this maximum is calculated by predicting salt concentration profiles as a function of current density and noting the current density at which the salt concentration at the cathode is zero. Another limitation arises when the salt concentration at the anode exceeds the solubility limit. Our analysis considers both possibilities. We have used Newman's concentrated solution theory to predict steady-state salt concentration profiles as a function of current density for mixtures of C8-DMC and LiFSI. These predictions were enabled by the complete electrochemical characterization of these mixtures (i.e., measurement of κ, D, t_{+}^{0}, and T_f as functions of salt concentration) that was reported in ref. 19. An interesting feature of these electrolytes is that t_{+}^{0} is negative across all salt concentrations. The dc potential across Li symmetric cells containing C8-DMC/LiFSI was measured experimentally as a function of applied current density and salt concentrations. At high enough current densities, clear signatures of the limiting current were observed. The experimentally determined limiting current was a non-monotonic function of salt concentration. It increases with increasing salt concentration up to m_{av} = 0.94 mol/kg and decreases with increasing salt concentration at higher values of m_{av}. The solubility limit of LiFSI in C8-DMC is 2.03 mol/kg. Our theoretical analysis indicates that the limiting current, up to m_{av} = 0.88

1mol/kg, occurs due to depletion of salt at the cathode, while the limiting
2current at higher values of m_{av} occurs due to the salt saturation at the anode.
3The experimentally determined time dependence of the potential across the
4lithium symmetric cells was also compared to predictions based on
5Newman’s concentrated solution theory. Our approach enables comparing
6theory with experiment with no adjustable parameters.
7

Conflicts of interest

There are no conflicts to declare.

Acknowledgements

This work was intellectually led by the Joint Center for Energy Storage Research (JCESR), an Energy Innovation Hub funded by the U.S. Department of Energy (DOE), Office of Science, Basic Energy sciences (BES), under Contract No. DEAC02-06CH11357. Early work by D.B.S. was supported by the National Science Foundation, grant number 1505669, under the SusChEM initiative. We thank Dr. Kevin R. Olson, Dr. Sue J. Mecham, and Prof. Joseph M. DeSimone for their helpful guidance in synthesizing C8-DMC.

References

1. N. Dey and B. P. Sullivan, *J. Electrochem. Soc.*, 1970, 117, 222.
2. J. Hong, H. Maleki, S. Al Hallaj, L. Redey and J. R. Selman, *J. Electrochem. Soc.* 1998, 145, 1489–1501.
3. D. H. C. Wong, J. L. Thelen, Y. Fu, D. Devaux, A. A. Pandya, V. S. Battaglia, N. P. Balsara and J. M. DeSimone, *Proc. Natl. Acad. Sci.*, 2014, 111, 3327–3331.
4. M. Chintapalli, K. Timachova, K. R. Olson, S. J. Mecham, D. Devaux, J. M. Desimone and N. P. Balsara, *Macromolecules*, 2016, 49, 3508–3515.
5. D. B. Shah, K. R. Olson, A. Karny, S. J. Mecham, J. M. DeSimone and N. P. Balsara, *J. Electrochem. Soc.*, 2017, 164, A3511–A3517.
6. J. H. Baik, D. G. Kim, J. H. Lee, S. Kim, D. G. Hong and J. C. Lee, *J. Ind. Eng. Chem.*, 2018, 64, 453–460.
7. T. Achiha, T. Nakajima, Y. Ohzawa, M. Koh, A. Yamauchi, M. Kagawa and H. Aoyama, *J. Electrochem. Soc.*, 2009, 156, A483.
8. Z. Zhang, L. Hu, H. Wu, W. Weng, M. Koh, P. C. Redfern, L. A. Curtiss and K. Amine, *Energy Environ. Sci.*, 2013, 6, 1806.
9. C. Wang, S. Tang, X. Zuo, X. Xiao, J. Liu and J. Nan, *J. Electrochem. Soc.*, 2015, 162, A1997–A2003.
10. J. Newman and K. E. Thomas-Alyea, *Electrochemical Systems*, John Wiley & Sons, Inc., Hoboken, New Jersey, 2004.
11. J. W. Park, K. Yoshida, N. Tachikawa, K. Dokko and M. Watanabe, *J. Power Sources*, 2011, 196, 2264–2268.

112. S. I. Lee, U. H. Jung, Y. S. Kim, M. H. Kim, D. J. Ahn and H. S. Chun, *Korean J. Chem. Eng.*, 2002, 19, 638–644.

313. Y. Ma, M. Doyle, T. F. Fuller, M. M. Doeff, L. C. De Jonghe and J. Newman, *J. Electrochem. Soc.*, 1995, 142, 1859.

514. D. M. Pesko, K. Timachova, R. Bhattacharya, M. C. Smith, I. Villaluenga, J. Newman and N. P. Balsara, *J. Electrochem. Soc.*, 2017, 164, E3569–E3575.

815. I. Villaluenga, D. M. Pesko, K. Timachova, Z. Feng, J. Newman, V. Srinivasan and N. P. Balsara, *J. Electrochem. Soc.*, 2018, 165, A2766–A2773.

1116. M. M. Doeff, L. Edman, S. E. Sloop, J. Kerr and L. C. De Jonghe, *J. Power Sources*, 2000, 89, 227–231.

1317. P. Georén and G. Lindbergh, *Electrochim. Acta*, 2001, 47, 577–587.

1418. D. M. Pesko, Z. Feng, S. Sawhney, J. Newman, V. Srinivasan and N. P. Balsara, *J. Electrochem. Soc.*, 2018, 165, 3186–3194.

1619. D. B. Shah, H. Q. Nguyen, L. S. Grundy, K. R. Olson, S. J. Mecham, J. M. Desimone and N. P. Balsara, *Phys. Chem. Chem. Phys.*, 2019, 21, 7857–7866.

1920. K. R. Olson, D. H. C. Wong, M. Chintapalli, K. Timachova, R. Januszewicz, W. F. M. Daniel, S. Mecham, S. Sheiko, N. P. Balsara and J. M. DeSimone, *Polymer*, 2016, 100, 126–133.

2221. J. Evans, C. A. Vincent and P. G. Bruce, *Polymer*, 1987, 28, 2324–2328.

2322. P. G. Bruce and C. A. Vincent, *J. Electroanal. Chem.*, 1987, 225, 1–17.

123. N. P. Balsara and J. Newman, *J. Electrochem. Soc.*, 2015, 162, A2720–A2722.

324. M. Doyle and J. Newman, *J. Electrochem. Soc.*, 1995, 142, 3465–3468.

425. M. Doyle, T. F. Fuller and J. Newman, *Electrochim. Acta*, 1994, 39, 2073–2081.

626. J. A. Maslyn, W. S. Loo, K. D. McEntush, H. J. Oh, K. J. Harry, D. Y. Parkinson and N. P. Balsara, *J. Phys. Chem. C*, 2018, 122, 26797–26804.

927. P. Barai, K. Higa and V. Srinivasan, *Phys. Chem. Chem. Phys.*, 2017, 19, 20493–20505.

1128. P. Bai, J. Li, F. R. Brushett and M. Z. Bazant, *Energy Environ. Sci.*, 2016, 9, 3221-3229.

Nomenclature

A	Active surface area of electrode (cm^2)
c	Concentration (mol/cm^3)
D	Salt diffusion coefficient of electrolytic phase (cm^2/s)
D_s	Salt diffusion coefficient of electrolyte in separator (cm^2/s)
F	Faraday's constant (96,485 C/mol)
i_{ss}	Steady-state current density (mA/cm^2)
i_{limit}	Limiting current density (mA/cm^2)
$i_{limit,sat}$	Limiting current density due to salt precipitation (mA/cm^2)
L	Thickness of electrolyte/separator (cm)
m	Molality (mol/kg)
R	Ideal gas constant (J/mol K)
R_i	Resistance of electrolyte/electrode interface when i_{ss} is reached (Ω)
T	Temperature (K)
T_f	Thermodynamic factor
t	Time (s)
$t_{+¿^0¿}$	Cation transference number relative to the solvent velocity. Obtained using the Balsara and Newman method
$t_{-¿^0¿}$	Anion transference number relative to the solvent velocity; $t_{-¿^0=1-t_{+¿^0¿}}$
$t_{+,id}$	Ideal transference number using steady-state current method
x	Position (cm)
$z_{-¿¿}$	Anion charge
$1+\frac{dln\gamma_{\pm}}{dlnm}$	Thermodynamic factor

Greek

$\gamma_{\pm}$	Mean molal activity coefficient of the salt
κ	Conductivity of the electrolytic phase; (S/cm)
κ_s	Conductivity of the electrolyte and separator combined; (S/cm)
v_i	Number of cations/anions per molecule of salt ($i=+\text{or}-¿$)
Φ	Electrolyte potential (mV)
Φ_{exp}	Experimental electrolyte potential (mV)
$\Phi_{measured}$	Measured cell potential (mV)
Φ_0	Steady-state model predicted electrolyte potential taken at x = 0 (mV)

Φ_1	Potential of the electrolyte at the electrode boundary for the transient model (mV)

1**Table of Contents Graphic**

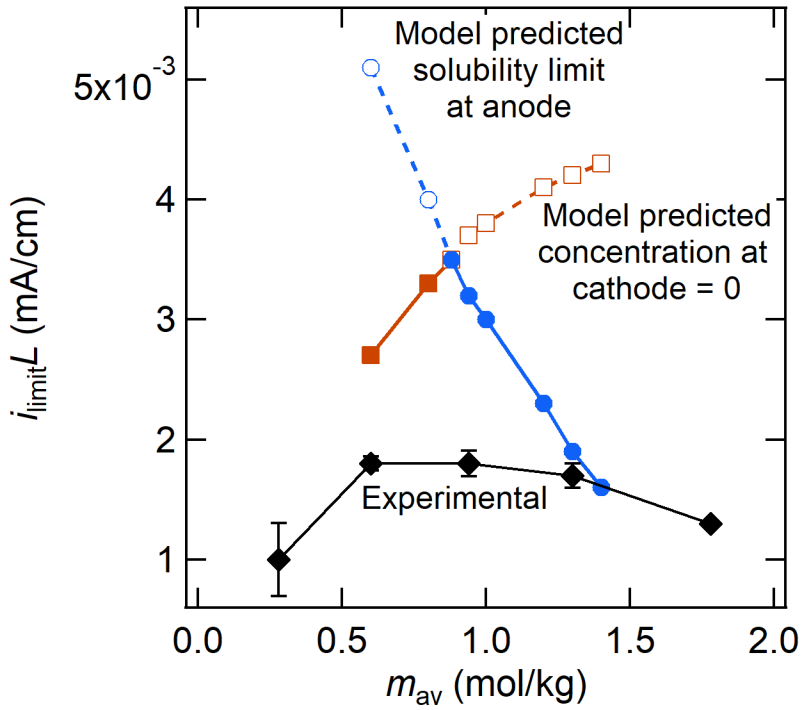

2